DSCC2019-9016

LOCOMOTION OF AN ORIGAMI INSPIRED NONHOLONOMIC SYSTEM

Vitaliy Fedonyuk

Department of Mechanical Engineering Clemson University Clemson, SC 29634 Email: vfedony@g.clemson.edu

Suyi Li

Department of Mechanical Engineering Clemson University Clemson, SC 29634 Email: suyil@clemson.edu

Priyanka Bhovad

Department of Mechanical Engineering Clemson University Clemson, SC 29634 Email: pbhovad@g.clemson.edu

Phanindra Tallapragada*

Department of Mechanical Engineering Clemson University Clemson, SC 29634 Email: ptallap@clemson.edu

ABSTRACT

Origami mechanisms are simple, lightweight, and can possess unique mechanical properties such as nonlinear tunable stiffness and multi-stability. Many studies have examined the use of these mechanical properties for adaptive and multi-functional structures and material systems. However, there are very few studies on how to exploit the mechanical properties of origami to generate or improve the locomotion of mobile robots. In this paper, we investigate the locomotion dynamics of a model origami robot system consisting of a bistable origami structure known as the generalized Kresling pattern attached to a Chaplygin sleigh, a canonical nonholonomic wheeled system. By applying a periodic torque on the Kresling segment we show that locomotion on a circle can be produced through the intrawell oscillations of the origami pattern. Furthermore, the bistability of Kresling pattern can be exploited to change the radius and speed of travel, producing two distinct modes of motion; and a control method is designed to switch the robot between these two modes. To the authors' knowledge this is the first such study of dynamic locomotion using origami.

1 INTRODUCTION

Origami is an ancient art of paper folding. One can create complex 3-D structures and mechanisms by simply folding a 2-D flat sheet along the prescribed fold lines. Fabrication of such complex shapes via traditional manufacturing techniques would indeed be very difficult if not impossible. The principle of origami is geometric and scale-independent, thus one can essentially apply the same design to create micro to macro-scale mechanisms. The absence of bulky rigid linkages in origami makes the resultant mechanism extremely lightweight and simplified. In addition, many origami mechanisms exhibit exceptional properties such as, multi-stability [1–4], auxetics [3–5], tunable nonlinear stiffness [3,6,7], etc. In particular, a multi-stable system is one which possesses multiple stable equilibrium configurations and perturbations around any equilibrium configuration remain bounded in the absence of external inputs. Each of the stable configurations corresponds to a minima of the potential energy function associated with the mechanism. All these aforementioned properties make origami an attractive candidate for designing novel very high degree of freedom robots and mechanisms. Such origami systems can have many potential applications for robots that can slide, crawl and climb. In all such applications the origami robots would have to contend with non-

^{*}Address all correspondence to this author.

holonomic constraints.

Nonholonomic constraints play a key role in the dynamics of mobile robots due to the relationship between rolling motion and no slip constraints [8-11]. The study of nonholonomic systems mostly focuses on analyzing different versions of canonical nonholonomic systems such as the rolling coin [12], the roller racer [10,13] and the snakeboard [14–16]. One such system is the Chaplygin sleigh [17–19]. The Chaplygin sleigh can be thought of as a cart that has a knife edge which is not allowed to slip in the direction perpendicular to the line joining the wheel and the center of mass. Control of the Chaplygin sleigh via the motion of an internal heavy particle or a rotor has been studied in numerous works [20–23]. In [24–26] the motion of a Chaplygin sleigh due to an internal spring loaded rotor or a forced oscillating mass is shown to display a variety of qualitatively different dynamics ranging from asymptotic straight line motion to limit cycles and chaotic dynamics depending on several system parameters. In particular it was identified that bistable potential functions were an important controllable means to affect the motion of the nonholonomic system.

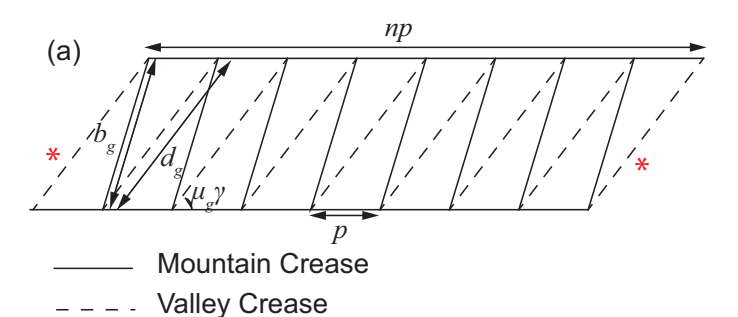
In this paper, we develop an equivalent Chaplygin sleighlike model for the locomotion of a bistable origami pattern called the generalized Kresling pattern. The origami system is modeled as a Chaplygin sleigh with an internal nonlinear oscillator. By using the nonlinear spring-like behaviors from the bistable Kresling origami, we show that intrawell oscillations of the Kresling pattern can cause the sleigh to travel in a circle on average. The radius and the average velocity of the circle are different when the Kresling pattern is oscillating around different equilibria. Moreover the physical space occupied by the mechanism is different in each of the two equilibrium configurations, with the mechanism moving faster in the larger configuration. We show that by taking advantage of the bistability of the Kresling pattern it is possible to switch the configuration of sleigh from the larger to the smaller one. Such switches in configuration are useful for a mobile robot that has to for instance navigate in narrow confined spaces.

The rest of this paper is organized as follows. In section 2 we introduce the generalized Kresling pattern and the experimental result showing the bistability of the structure. In section 3 we derive the equations of motion for the nonholonomic origami sleigh system using the Euler-Lagrange method. In section 4 we show the motion of the system due to periodic excitation and demonstrate interwell switching.

2 GENERALIZED KRESLING PATTERN

The "traditional" Kresling pattern was developed by Biruta Kresling [27] and its geometric design and bistability is extensively studied in literature [28–31]. It is designed as a flat-foldable mechanism, that is, its length at fully-contracted stable state is exactly zero. In this study, we use a "generalized"

Kresling pattern, which has a non-zero length at fully-contracted stable state [2]. This non-zero length is described by a new design parameter H, and it opens up a new design space for the Kresling pattern. Moreover, the generalized Kresling pattern can better accommodate the realistic sheet material thickness in its design.



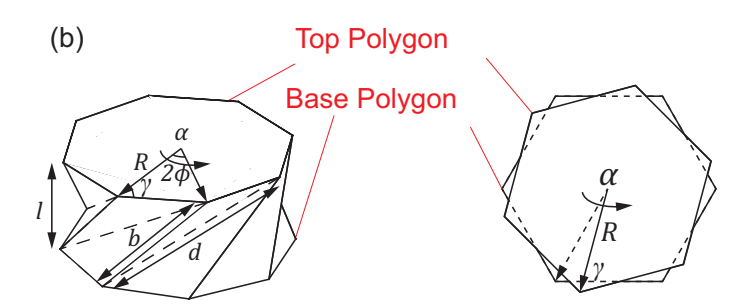


Figure 1: The design of the generalized Kresling pattern (a) Crease pattern depicting the design parameters. The creases marked with (*) are glued together to create a Kresling segment. (b) Isometric view and top view of folded Kresling segment depict the important geometric parameters and the sign convention for rotation angle α

The design parameters of the generalized Kresling pattern are: n (number of sides of the base and top polygon), p (side length of the base and top polygon), μ_i (angle ratio), and H (Kresling segment length at the fully-contracted stable state). The crease pattern is composed of equally spaced mountain and valley creases (Figure 1(a)). The first and last valley creases are glued together to generate an axisymmetric twisted polygonal prism (Figure 1(b)). The base and top of the cylinder create regular polygons that remain rigid during the folding motion. To design the generalized Kresling pattern, we start from the traditional Kresling, with its geometry given by

$$\phi = \frac{\pi}{n}, \quad R = \frac{p}{2\sin(\phi)}, \quad \gamma = \frac{\pi}{2} - \phi,$$

where ϕ is half the internal angle of the base and top polygon, R is the circumscribed radius of the base and top polygon, γ is the angle between the radius vector and polygon side as shown in

Figure 1 (b). The strain-free lengths of the valley and mountain creases are then given by

$$d_i = 2R\cos(\gamma - \mu_i \gamma),$$

$$b_i = \sqrt{p^2 + d_i^2 - 2pd_i\cos(\mu_i \gamma)}.$$

The top polygon of traditional Kresling segment is translated away from the bottom polygon by a distance of H to create the generalized Kresling. The resulting crease pattern is no longer flat-foldable; but retains an identical range of rotation as viewed from the top. The new strain-free lengths of valley and mountain crease and the angle of inclination of valley crease are given by

$$egin{aligned} d_g &= \sqrt{d_i^2 + H^2}, \ b_g &= \sqrt{b_i^2 + H^2}, \ \mu_g \gamma &= \cos^{-1}(rac{p^2 + d_g^2 - b_g^2}{2pd_g}). \end{aligned}$$

Here, the subscript i refers to the parameters for traditional Kresling and subscript g refers to those for generalized pattern. The angle of rotation (α) is used to characterize the folding motion of a segment (Figure 1 (b)). The length of the segment (l) is defined as the perpendicular distance between top and bottom polygon. The lengths of valley and mountain crease are then calculated as

$$d = \sqrt{2R^2(1 - \cos(\alpha + 2\phi)) + l^2},$$

$$b = \sqrt{2R^2(1 - \cos(\alpha)) + l^2}.$$
 (1)

From the fully-contracted geometry we can determine the upper limit for α to be, $\alpha_c = 2\mu_i \gamma$. The lower limit for α can be computed by setting the length b equal to the natural length b_g and solving for α .

$$\alpha_e = \{\min(\alpha) | b(\alpha) = b_g \}.$$

The mountain and valley creases in Kresling segment can be assumed as truss members connected by pin joints [31]. It can be assumed that the length of the valley crease (d) remains constant and only mountain crease (b) is compressed or stretched throughout the folding motion [28]. With this assumption, the derivative of d with respect to α is zero so that

$$l = \sqrt{H^2 + 2R^2(\cos(\alpha + 2\phi) - \cos(\alpha_c + 2\phi))}.$$
 (2)

Thus, we have closed form solutions for describing the folding kinematics. The strain (ε) and strain energy (U) due to folding can now be calculated as

$$\varepsilon = \frac{b}{b_g} - 1$$
, and $U = \frac{1}{2}K\varepsilon^2$,

where K is the material stiffness. For the purpose of this analysis we normalize the strain energy U by K, and define the non-dimensional strain energy as $E=\frac{1}{2}\epsilon^2$. The normalized strain energy of the Kresling segment is minimum at its two stable configurations (Figure 2). Thus, we have two distinct potential energy wells separated by a peak. This bistability in a Kresling segment arises due to the non-rigid foldable nature of the facets. That is, its facets are undeformed at the two stable states, but they have to undergo some deformation while folding between the two stable states. We will use this property of bistable generalized Kresling segment to get two distinct modes of locomotion in Chaplygin sleigh.

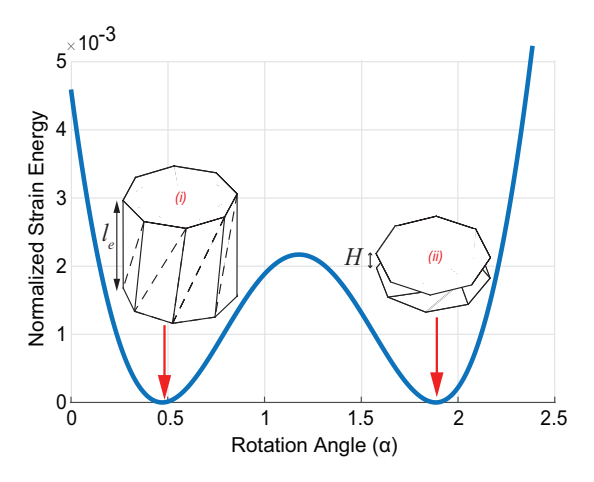


Figure 2: The normalized strain energy versus rotation angle for bistable generalized Kresling segment. (i) denotes fully-extended stable state, $l_e = l(\alpha_e)$ and (ii) denotes fully-contracted stable state. n = 8, p = 30 mm, $\mu_i = 0.8$ and H = 20 mm

2.1 EXPERIMENTAL RESULTS

We have experimentally verified the bistability of generalized Kresling segment. The experimental setup is shown in Figure 3. The tests were performed on ADMET Universal Testing Machine (eXpert 5601). The generalized Kresling segment was fabricated from paper (Daler - Rowney Canford 150 gsm). First, the 2-D drawing of the pattern was prepared in the Solidworks® software. This pattern was then cut out of the paper with perforated creases using CricutMaker®. Additional reinforcement triangles were attached to the triangular facets using double sided tape. Finally, the segment was folded by hand and the top and bottom polygons were attached to the segment using double sided tape. A custom rotation fixture was designed using dual ball-bearing hub to allow for free rotation of one end of the Kresling segment. One end of the Kresling segment was fixed to the rotation fixture mounted on the lower base plate and the other end was fixed to the upper platen.

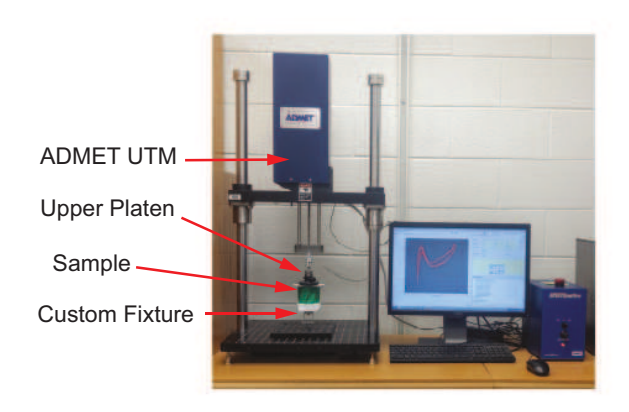


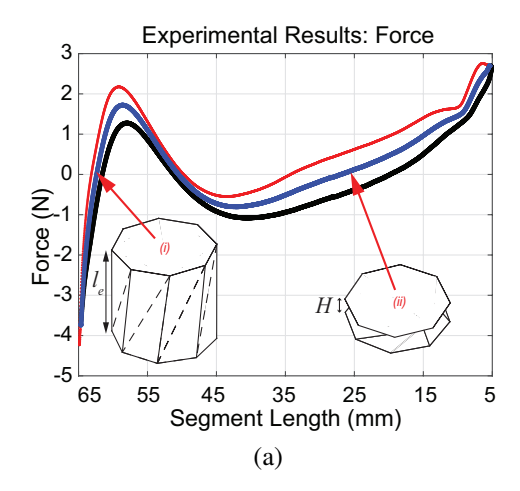
Figure 3: Experimental setup for verification of bistability for generalized Kresling segment

Some modifications to the pattern were deemed necessary in the fabrication of Kresling segment. During the initial testing it was observed that excessive stresses were developing along the mountain creases. This caused the bistable segment to tear after a few cycles of testing. Thus, the mountain creases were cut to allow smooth folding motion of the segment. A similar approach is used in literature, where the resulting pattern is called Flexigami [32]. Additionally, triangular reinforcements were added to the triangular facets to increase their relative stiffness compared to creases and get stronger bistability. The elasticity of paper, fabrication defects, contact between the deforming triangular facets, and internal friction cause the contraction and extension path to vary slightly. As a result, we see a hysteresis loop forming instead of a single curve for force versus displacement as seen in analytical prediction. The bistable nature of the generalized Kresling segment is evident from the Figure 4.

3 EQUATIONS OF MOTION

In this section we develop model of a Chaplygin sleigh like nonholonomic system based on the Kresling origami pattern. The Chaplygin sleigh is modeled as vertical plate connected to the wheel via a rigid arm. The sleigh has mass m_c and moment of inertia I_1 . The sleigh has a nonholonomic constraint applied to point P on the wheel which does not allow motion in the Y_b direction (Figure 5(a)). The Kresling segment is mounted on the sleigh such that its base and top polygon are perpendicular to the (x,y) plane and segment's axis of rotation is aligned with Y_b (Figure 5(b)). One face of the segment is fixed to the Chaplygin sleigh and the other face is free to rotate about its rotation axis. The torque (τ) is applied to the free face about Y_b axis. This face is weighted with mass m_k and moments of inertia about the z axis and its own axis are I_2 and I_3 respectively.

The system has a configuration manifold $SE(2) \times S^1$ parameterized by $q = [x, y, \theta, \alpha]^T$ where (x, y) is the position of the



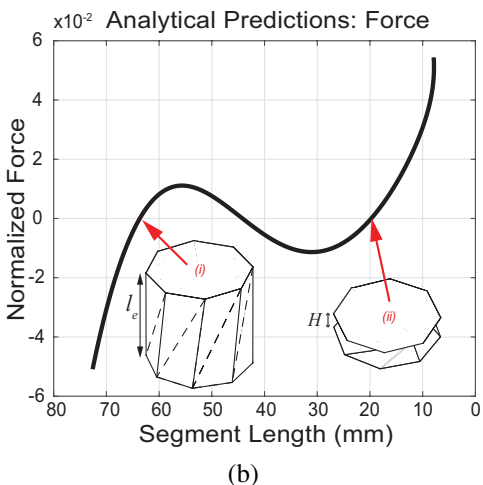


Figure 4: Verification of the bistability of Kresling segment (a)Experimental results: Force versus segment length. Red line represents reaction force under contraction and the black line represents reaction force under extension. The blue line is the averaged reaction force. (b) Analytical predictions: Normalized force versus segment length. (i) denotes the fully-extended stable state, $l_e = l(\alpha_e)$ and (ii) denotes the fully-contracted stable state. n=8, p=30 mm, $\mu_i=0.8$, H=20 mm

sleigh, θ is the orientation and α is the rotation angle of the Kresling segment. The positions and velocities of the free face can be written as

$$x_k = x - l(\alpha)\sin(\theta)$$
$$y_k = y + l(\alpha)\cos(\theta)$$

and

$$\dot{x}_k = \dot{x} - \dot{l}(\alpha, \dot{\alpha})\sin(\theta) - l(\alpha)\dot{\theta}\cos(\theta)$$
$$\dot{y}_k = \dot{y} + \dot{l}(\alpha, \dot{\alpha})\cos(\theta) - l(\alpha)\dot{\theta}\sin(\theta).$$

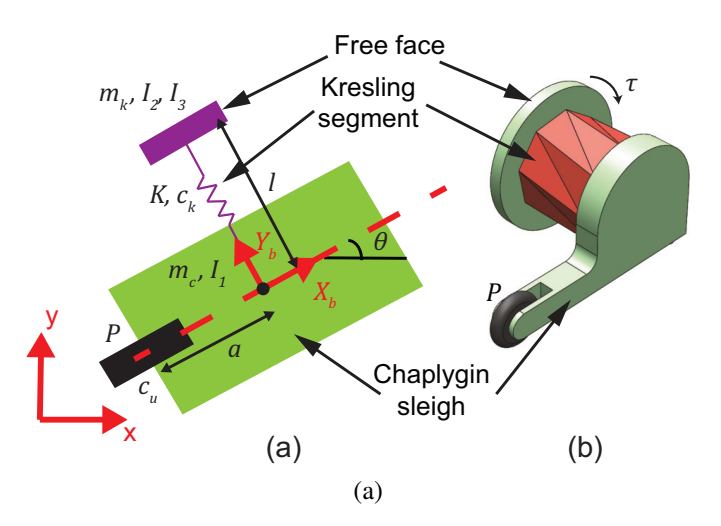


Figure 5: Origami inspired Chaplygin sleigh: (a) Schematic of the system depicting design parameters and co-ordinate systems (b) 3D visualization of the origami sleigh. The nonholonomic constraint is applied to the sleigh at point P.

The Lagrangian of the system (\mathcal{L}) is then given by

$$\mathcal{L} = \frac{1}{2}m_c(\dot{x}^2 + \dot{y}^2) + \frac{1}{2}m_k(\dot{x_k}^2 + \dot{y_k}^2) + \frac{1}{2}(I_1 + I_3 + ml^2)\dot{\theta}^2 + \frac{1}{2}I_2\dot{\alpha}^2 - U(\alpha)$$

The system must satisfy the nonholonomic constraint that the velocity of point P parallel to the origami structure is zero

$$-\sin(\theta)\dot{x} + \cos(\theta)\dot{y} - b\dot{\theta} = 0.$$

with Pfaffian one form being

$$-\sin\theta dx + \cos\theta dy - bd\theta = 0. \tag{3}$$

The system is also subject to Raleigh dissipation modeled by the dissipation function

$$\mathcal{R} = \frac{1}{2}c_u u^2 + \frac{1}{2}c_k \dot{l}^2$$

where u is the velocity of point P in the axis pointing to the center of mass and c_k is the damping in the Kresling pattern. The Euler-Lagrange equations are

$$\frac{d}{dt}\left(\frac{\partial \mathcal{L}}{\partial \dot{q}_k}\right) - \frac{\partial \mathcal{L}}{\partial q_k} = \mathcal{W}_k \lambda + \Gamma_i + \tau_i(t)$$

where λ_j is the Lagrange multiplier corresponding to the jth constraint, \mathcal{W}_k is the coefficient of the one form dq_k in (3), $\Gamma_i = -\frac{\partial \mathcal{R}}{\partial q_i}$ is the dissipation force, and $\tau_i = [0,0,0,\tau]^T$ is the applied torque. In our analysis we use a periodic torque of the form $\tau = A\cos(\Omega t)$. Straight forward calculations yield the Euler-Lagrange equations as

$$\begin{bmatrix} \mathcal{M} - \mathcal{W}^T \\ \mathcal{W} & 0 \end{bmatrix} \begin{bmatrix} \ddot{q} \\ \lambda \end{bmatrix} = \mathcal{B}(q, \dot{q}) \tag{4}$$

where

$$\mathcal{B}(q,\dot{q}) = egin{bmatrix} \mathcal{C}(q,\dot{q})\dot{q} \ \dot{\mathcal{W}}\dot{q} \end{bmatrix} + rac{\partial \mathcal{L}}{\partial q} + au.$$

The matrix $C(q,\dot{q})$ contains elements $c_{jk} = \sum_{i=1}^n c_{ijk}\dot{q}_i$ where c_{ijk} are the Christoffel symbols of the first kind computed as $c_{jk} = \sum_{i=1}^n \frac{1}{2} (\frac{\partial \mathcal{M}_{kj}}{\partial q_i} + \frac{\partial \mathcal{M}_{ki}}{\partial q_j} - \frac{\partial \mathcal{M}_{ij}}{\partial q_k}) \dot{q}_i$. The fifth equation of (4) is obtained by differentiating the nonholonomic constraint with respect to time. This is needed to complete the system in this form and solve for the velocities. In our formulation we eliminate the constraint force using gaussian elimination in order to obtain the equations in matrix form useful for fixed points analysis. Let us define the body-fixed state vector $\boldsymbol{\xi} = [u, \omega_1, \omega_2, \alpha]^T$ where u is the velocity of P, $\omega_1 = \dot{\theta}$, and $\omega_2 = \dot{\alpha}$. The velocities and accelerations of the tail may first be expressed in terms of u, ω_1 and θ as

$$\dot{x} = u\cos\theta$$
$$\dot{y} = u\sin\theta$$

and

$$\ddot{x} = \dot{u}\cos\theta - u\omega_1\sin\theta$$
$$\ddot{y} = \dot{u}\sin\theta + u\omega_1\cos\theta.$$

After substituting the above expressions into (4) and eliminating λ the following reduced equations are obtained.

$$\begin{bmatrix} \mathcal{M}_b(\alpha) & 0 \\ 0 & 1 \end{bmatrix} \dot{\xi} = \begin{bmatrix} f_1(u, \omega_1, \omega_2, \alpha) \\ f_2(u, \omega_1, \omega_2, \alpha) \\ f_3(u, \omega_1, \omega_2, \alpha) \end{bmatrix}$$
 (5)

where f_1 , f_2 , f_3 and the elements of $M_b(\alpha)$ are described in the appendix.

4 DYNAMICS OF THE ORIGAMI SLEIGH WITH PERI-ODIC ACTUATION

We simulate the equations of motion (5) under the effect of a periodic torque τ . The origami robot exhibits limit cycle motion

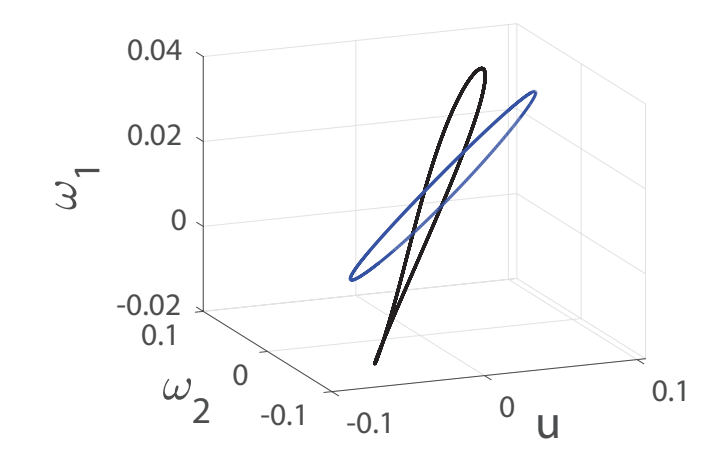
for a large range of parameters and control inputs. Although the system may also exhibit chaos in the presence of large interwell oscillations, we focus on control of the mobile robot through intrawell oscillations exploiting the bistability of the origami structure to achieve multiple motion regimes. Since the origami structure will exhibit this bistability for a large range of parameters, we chose different parameters in the robot design than those used in the experiment. However we emphasize that origami is scalable making the units and scale of motion less relevant for our analysis. Limit cycle motion of the system is shown in Figure 6. Each of the velocities oscillates with the same frequency as that of the input making the limit cycle a loop in the (u, ω_1, ω_2) space as shown in Figure 6(c). Let us define $(\bar{u}, \bar{\omega_1}, \bar{\omega_2})$ to be the average values of the velocities over one time period on the limit cycle. We find that $\bar{u} > 0$ and $\bar{\omega}_1 > 0$ making the limit cycle motion in the (x, y) plane a circle on average as seen in Figure 6(a).

We find that the average values of all the limit cycle velocities change for each equilibrium position. When $\alpha(0) = \alpha_e$ we get $\bar{u}=1.75\times 10^{-2}, \ \bar{\omega}_1=1.47\times 10^{-2}$ and $\bar{\omega}_2=0$ whereas for $\alpha(0) = \alpha_c$ we get $\bar{u} = 4.15 \times 10^{-3}$, $\bar{\omega}_1 = 7.94 \times 10^{-3}$ and $\bar{\omega}_2 = 0$. We find that when the Kresling segment rotation angle is close to α_e at which the segment is fully-extended we get both a higher \bar{u} and $\bar{\omega}$; which means the sleigh absorbs more of the energy from the input torque in this position. The radius of motion in the (x,y) plane, however, depends on both of these. A similar effect is shown analytically for the elastic Chaplygin sleigh analyzed in [26] For this reason we see from Figure 6(a) that the radius for $\alpha(0) = \alpha_c$ is actually smaller despite $\bar{\omega}_1$ being lower. We also find that in the fully-extended position, the robot occupies more space (Figures 6(d) and (e)). This becomes another tradeoff for the robot moving faster in this configuration. Based on the required task the robot is able to move faster, with a larger radius while occupying more space or move on a tight circle as a smaller robot.

In order to make use of the bistability we must be able force the Kresling segment to transition from one potential well to another. Since α and l are mutually increasing and decreasing, a torque on the free face of the segment can be efficiently used to transition the segment to the other potential well. We show that this can be done with PD control. The proportional term allows us to define the desired potential well and the derivative term serves to compound with dissipation to decrease the convergence rate of the response. When we require the segment to transition wells; we switch off the periodic input and apply a control law of the form

while
$$(|\alpha - \alpha_d| > e)$$
 do
$$\tau = -K_p(\alpha - \alpha_d) - K_d\omega_2$$
 end while

where e is some chosen small error, $\alpha_d \in \{\alpha_e, \alpha_c\}$ is the desired value of the Kresling segment rotation angle and K_p and K_d are



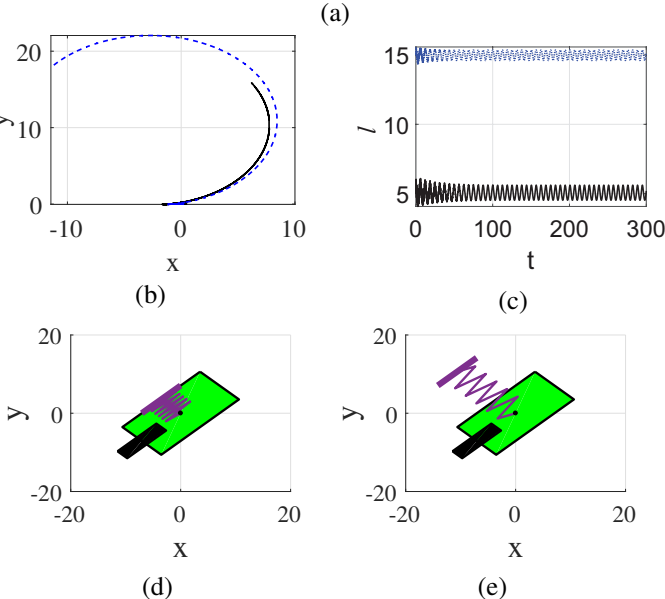


Figure 6: Sleigh response to periodic torque with A=100, and $\Omega=1$. Initial conditions are all zero except $\alpha(0)=\alpha_e$ for the blue dashed trajectory and $\alpha(0)=\alpha_c$ for the black solid lines in each subfigure. (a) The limit cycle in the velocity space, (b) The trajectory of the sleigh in the (x,y) plane, (c) The length of the Kresling segment versus time, (d) schematic of the system in the fully-contracted position and (e) schematic of the sleigh in the fully-extended position. The geometry of the Kresling segment are n=8, p=7, H=5, and $\mu_i=0.8$ with stiffness $K=5\times 10^4$ and damping $c_k=1$. Other parameters are $m_1=0.5$, $m_2=0.5$, $m_1=1$, $m_2=1$, $m_2=1$, $m_1=1$, $m_2=1$, $m_1=1$, $m_2=1$, $m_2=1$, $m_1=1$, $m_1=1$, $m_2=1$, $m_1=1$, $m_2=1$, $m_1=1$, $m_2=1$, $m_1=1$, $m_1=1$, $m_1=1$, $m_2=1$, $m_1=1$, $m_1=1$, $m_2=1$, $m_1=1$, $m_2=1$, $m_1=1$, $m_2=1$, $m_1=1$, $m_1=1$, $m_1=1$, $m_1=1$, $m_2=1$, $m_1=1$

coefficients for the controller. The controller gains must be large enough to force a transition over the unstable position. The exact values required depend on initial conditions so we simply chose large values and show that that the control input is still of the same order as the periodic input. The feedback control law

allows us to switch wells immediately even while the sleigh is moving. We first show a transition with zero initial conditions to focus on the dynamics of this controller.

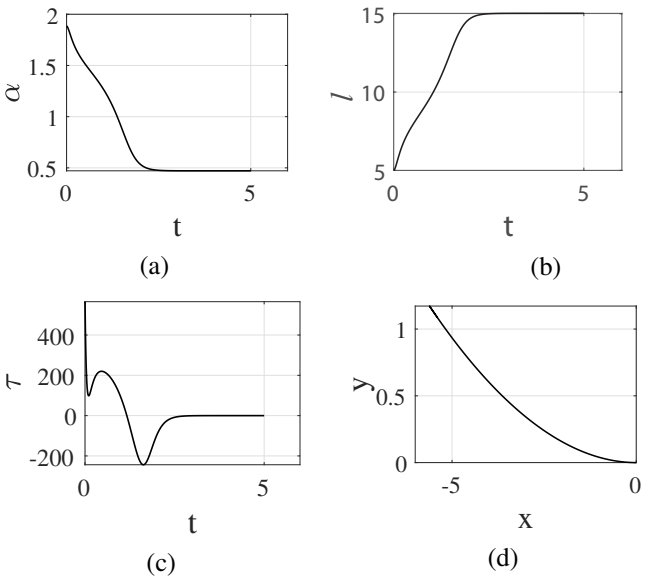


Figure 7: Sleigh transition procedure with $K_p = 400$ and $K_d = 400$. Initial conditions are all zero except $\alpha(0) = \alpha_c$. (a) The angle of rotation of the Kresling segment, (b) The length of the Kresling segment (c) Applied torque and (d) The trajectory in the (x,y) plane. The geometry of the Kresling segment are n = 8, p = 7, H = 5, and $\mu_i = 0.8$ with stiffness $K = 5 \times 10^4$ and damping $c_k = 1$. Other parameters are $m_1 = 0.5$, $m_2 = 0.5$, $I_1 = I_2 = I_3 = 0.01$, a = 10 and $c_u = 0.1$.

In Figure 7(a) and (b) we see that the segment is able to smoothly transition from one equilibrium position to the other in under 5 seconds. Figure 7(c) shows that the input required to transitions is of the same order as the sinusoidal input we use to steer the sleigh. The response of the sleigh itself is seen in Figure 7(d).

A simulation of the control law is shown in Figure 8. The sleigh begins with $\alpha(0) = \alpha_c$ and we apply a periodic input with A=100 and $\Omega=1$ for $t\in[0,300)$ and then the origami sleigh is required to transition to the other stable configuration using the transition procedure. We then apply the same periodic input until t=600. We see that during the first three hundred seconds the sleigh first travels backward briefly during the transient phase and then travels along a circle with $\bar{u}=4.15\times10^{-3}$ and $\bar{\omega}_1=7.94\times10^{-3}$ (Figure 8(a)). The system then transitions to the other stable configuration. Once the periodic input starts again we see another transient phase where u is on average less than zero before the sleigh settles to a limit cycle with $\bar{u}=1.75\times10^{-2}$ and $\bar{\omega}_1=1.47\times10^{-2}$. The system can therefore change its speed and radius travel using the torque on the Kresling segment as the only control input.

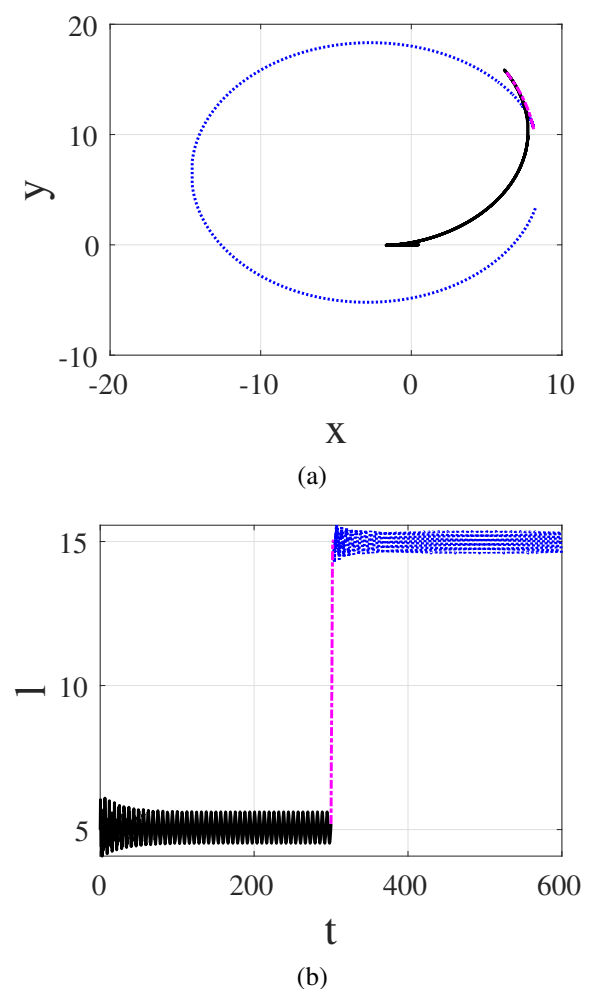


Figure 8: Robot switching from the fully-contracted position to the fully-extended potion. Oscillations about the fully-contracted position are shown in black lines, the transition in magenta dash-dotted lines and oscillations about the fully-extended position in blue dashed lines. (a) The trajectory in the plane. (b) The length of the Kresling segment. The geometry of the Kresling segment are n = 8, p = 7, H = 5, and $\mu_i = 0.8$ with stiffness $K = 5 \times 10^4$ and damping $c_k = 1$. Other parameters are $m_1 = 0.5$, $m_2 = 0.5$, $I_1 = I_2 = I_3 = 0.01$, $I_1 = I_2 = I_3 = 0.01$, $I_2 = I_3 = 0.01$, $I_3 = I_3 = 0.01$, $I_4 = I_3 = 0.01$.

5 SUMMARY AND CONCLUSION

This study focuses on exploiting the bistability of an origami mechanism to control the motion of the Chaplygin sleigh. We analyzed the motion of a Chaplygin sleigh mounted with an origami structure known as the generalized Kresling pattern. Applying a periodic torque to the Kresling segment produces periodic intrawell oscillations in its length. This in turn gives rise to limit cycle motion of the Chaplygin sleigh. This motion is such that the trajectory is a circle on average in the (x, y) plane. The radius and speed of travel along this circular trajectory, and the size of the robot can change based on which equilibrium position the

Kresling segment is oscillating about.

We have also shown that the system is able to transition from one equilibrium position to the other smoothly by using a feedback control law. This means that the single input of a periodic torque on the Kresling segment is able to generate two regimes of motion and switch between them. Hence, We are able to reduce the complexity of the control architecture for the robot actuation. The physical size of the robot also decreases on demand allowing the robot to navigate smaller spaces.

To the best of the authors' knowledge this is the first paper on the dynamics of a mobile origami mechanism with non-holonomic constraints. The results obtained here lay the groundwork for the design of highly adaptive, lightweight, multi-stable origami robots that can find applications in many areas such as search and rescue, inspection, and medical applications. With the recent findings that nonholonomic constraints govern fish-like swimming [33–35], origami based mechanisms can also be expected to play a significant role in designing efficient and agile aquatic robots. The design and fabrication of the origami robot working on these principles will be taken up as a future work.

6 ACKNOWLEDGEMENT

P. Bhovad and S. Li acknowledge the partial support from the National Science Foundation (Award # CMMI-1633952 and CMMI-1751449 CAREER). V. Fedonyuk and P. Tallapragada acknowledge the partial support from the NSF grant CMMI 1563315.

REFERENCES

- [1] Li, S., and Wang, K. W., 2015. "Fluidic origami with embedded pressure dependent multi-stability: a plant inspired innovation". *Journal of The Royal Society Interface*, 12(111), p. 20150639.
- [2] Bhovad, P., and Li, S., 2018. "Using multi-stable origami mechanism for peristaltic gait generation: A case study". In ASME 2018 International Design Engineering Technical Conferences and Computers and Information in Engineering Conference, American Society of Mechanical Engineers, pp. V05BT07A061-V05BT07A061.
- [3] Li, S., Fang, H., Sadeghi, S., Bhovad, P., and Wang, K.-W., 2019. "Architected origami materials: How folding creates sophisticated mechanical properties". *Advanced Materials*, *31*(5), p. 1805282.
- [4] Yasuda, H., and Yang, J., 2015. "Reentrant origami-based metamaterials with negative Poisson's ratio and bistability". *Physical Review Letters*, *114*(18), pp. 1–5.
- [5] Schenk, M., and Guest, S. D., 2011. "Origami folding: A structural engineering approach". In Origami 5 Fifth International Meeting of Origami Science Mathematics and Education, pp. 1–16.
- [6] Filipov, E. T., Tachi, T., and Paulino, G. H., 2015. "Origami tubes assembled into stiff, yet reconfigurable structures and

- metamaterials". *Proceedings of the National Academy of Sciences*, 112(40), oct, pp. 12321–12326.
- [7] Li, S., and Wang, K. W., 2015. "Fluidic origami: a plant-inspired adaptive structure with shape morphing and stiffness tuning". *Smart Materials and Structures*, **24**(10), p. 105031.
- [8] Bloch, A. M., Krishnaprasad, P. S., Marsden, J. E., and Murray, R. M., 1996. "Nonholonomic Mechanical Systems with Symmetry". *Archive for Rational Mechanics and Analysis*, 136, pp. 21–99.
- [9] Murray, R. M., and Sastry, S. S., 1991. "Steering nonholonomic systems in chained form". In Decision and Control, 1991., Proceedings of the 30th IEEE Conference on, IEEE, pp. 1121–1126.
- [10] Bullo, F., and Žefran, M., 2002. "On mechanical control systems with nonholonomic constraints and symmetries". *Systems & Control Letters*, **45**(2), pp. 133–143.
- [11] Bloch, A. M., 2003. *Nonholonomic Mechanics and Control*. Springer Verlag.
- [12] McDonald, A. J., and McDonald, K. T., 2000. "The rolling motion of a disk on a horizontal plane". *arXiv preprint physics/0008227*.
- [13] Bizyaev, I. A., 2017. "The inertial motion of a roller racer". *Regular and Chaotic Dynamics*, **22**(3), pp. 239–247.
- [14] Ostrowski, J., Lewis, A., Murray, R., and Burdick, J., 1994. "Nonholonomic mechanics and locomotion: the snakeboard example". In Proceedings of the Control and Decision Conference, pp. 2391–2397.
- [15] Ostrowski, J. P., Desai, J. P., and Kumar, V., 2000. "Optimal gait selection for nonholonomic locomotion systems". *The International journal of robotics research*, *19*(3), pp. 225–237.
- [16] Dear, T., Kelly, S. D., Travers, M., and Choset, H., 2015. "Snakeboard motion planning with viscous friction and skidding". In Robotics and Automation (ICRA), 2015 IEEE International Conference on, IEEE, pp. 670–675.
- [17] Chaplygin, S. A., 2008. "On the theory of the motion of nonholonomic systems: The reducing multiplier theorem.". *Translated version in Regular and Chaotic Dynamics*.
- [18] Neimark, J. I., and Fufaev, N. A., 1972. *Dynamics of Non-holonomic systems*. AMS.
- [19] Borisov, A. V., and Mamaev, I. S., 2009. "The dynamics of a chaplygin sleigh". *Journal of Applied Mathematics and Mechanics*, 73(2), pp. 156–161.
- [20] Osborne, J. M., and Zenkov, D. V., 2005. "Steering the chaplygin sleigh by a moving mass". In Proceedings of the American Control Conference.
- [21] Kelly, S. D., Fairchild, M. J., Hassing, P. M., and Tallapragada, P., 2012. "Proportional heading control for planar navigation: The chaplygin beanie and fishlike robotic swimming". In Proceedings of the American Control Con-

- ference.
- [22] Fedonyuk, V., and Tallapragada, P., 2018. "Sinusoidal control and limit cycle analysis of the dissipative chaplygin sleigh". *Nonlinear Dynamics*, pp. 1–12.
- [23] Tallapragada, P., and Fedonyuk, V., 2017. "Steering a chaplygin sleigh using periodic impulses". *Journal of Computational and Nonlinear Dynamics*.
- [24] Fedonyuk, V., and Tallapragada, P., 2018. "Chaotic dynamics of the chaplygin sleigh with a passive internal rotor". *Nonlinear Dynamics*.
- [25] Bizyaev, I. A., Borisov, A. V., and Kuznetsov, S. P., 2019. "The chaplygin sleigh with friction moving due to periodic oscillations of an internal mass". *Nonlinear Dynamics*, pp. 1–16.
- [26] Fedonyuk, V., and Tallapragada, P., 2019. "The dynamics of a chaplygin sleigh with an elastic internal rotor". *Regular and Chaotic Dynamics*, 24(1), pp. 114–126.
- [27] Kresling, B., 2008. "Natural twist buckling in shells: From the hawkmoths bellows to the deployable kresling-pattern and cylindrical miuraori". In Proceedings of the 6th International Conference on Computation of Shell and Spatial Structures, pp. 1–4.
- [28] Guest, S. D., and Pellegrino, S., 1994. "The folding of triangulated cylinders, part i: geometric considerations". *Journal of applied mechanics*, **61**(4), pp. 773–777.
- [29] Pagano, A., Yan, T., Chien, B., Wissa, A., and Tawfick, S., 2017. "A crawling robot driven by multi-stable origami". Smart Materials and Structures, 26(9), p. 094007.
- [30] Hunt, G. W., and Ario, I., 2005. "Twist buckling and the foldable cylinder: an exercise in origami". *International Journal of Non-Linear Mechanics*, **40**(6), pp. 833–843.
- [31] Jianguo, C., Xiaowei, D., Ya, Z., Jian, F., and Yongming, T., 2015. "Bistable behavior of the cylindrical origami structure with kresling pattern". *Journal of Mechanical Design*, *137*(6), p. 061406.
- [32] Nayakanti, N., Tawfick, S. H., and Hart, A. J., 2017. "Twist Coupled Kirigami Cellular Metamaterials and Mechanisms". *Extreme Mechanics Letters*.
- [33] Tallapragada, P., 2015. "A swimming robot with an internal rotor as a nonholonomic system". *Proceedings of the American Control Conference*.
- [34] Pollard, B., Fedonyuk, V., and Tallapragada, P., 2018. "Limit cycle behavior and model reduction of an oscillating fish-like robot.". In Proceedings of the ASME 2018 Dynamic Systems and Control Conference.
- [35] Pollard, B., and Tallapragada, P., 2017. "An aquatic robot propelled by an internal rotor.". *IEEE/ASME Transaction on Mechatronics*.

Appendix: Equations of motion expressions

The functions in equation (5) of section 3 are

$$\begin{split} f_1 &= -\frac{1}{b^3} \left(\left(b^3 (a(m_c + m_k) \omega_1^2 - c_u u) + \omega_1 \omega_2 r^2 m_2 (\sin(-\alpha + \alpha_c) r^2 + \sin(\alpha + 2\phi) H^2 + r^2 \sin(2\alpha + 4\phi) - r^2 \sin(\alpha + 4\phi + \alpha_c) \right) \right) \\ &+ (\alpha_c) + (\alpha_c$$

and $M_b(\alpha)$ has elements

$$\begin{split} M_b^{1,1} &= m_c + m_k \\ M_b^{1,2} &= \frac{m_k}{b^3} (-4H^2r^2\cos(\alpha_c + 2\phi) + 4H^2r^2\cos(\alpha + 2\phi) \\ &+ 2r^4(\cos(2\alpha_c + 4\phi) + \cos(2\alpha + 4\phi) - 2\cos(\alpha + 4\phi) \\ &+ (2\cos(2\alpha_c + 4\phi) + \cos(2\alpha + 4\phi) - 2\cos(\alpha + 4\phi) \\ &+ (2\cos(2\alpha_c + 4\phi) + 2\cos(2\alpha_c + 4\phi) + 4r^4 + 4r^4) \end{split}$$

$$\begin{split} M_b^{1,3} &= 0 \\ M_b^{2,1} &= -\frac{lm_k}{ab^3} (-4H^2r^2\cos(\alpha_c + 2\phi) + 4H^2r^2\cos(\alpha + 2\phi) \\ &+ 2r^4\cos(2\alpha_c + 4\phi) + 2r^4\cos(2\alpha + 4\phi) - 4r^4\cos(\alpha + 4\phi) \\ &+ (2\cos(2\alpha_c + 4\phi) + 2r^4\cos(2\alpha_c + 4\phi) - 4r^4\cos(\alpha + 4\phi) \\ &+ (2\cos(2\alpha_c + 4\phi) + 2r^4\cos(2\alpha_c + 4\phi) - 4r^4\cos(\alpha + 4\phi) \\ &+ (2\cos(2\alpha_c + 4\phi) + 2r^4\cos(2\alpha_c + 4\phi) - 4r^4\cos(\alpha + 4\phi) \\ &+ (2\cos(2\alpha_c + 2\phi)m_k + 4r^4 + 4r^4) \end{split}$$

$$\begin{split} M_b^{2,1} &= \frac{l}{a} (4\cos(\alpha + 2\phi)m_k r^2 - 4\cos(\alpha_c + 2\phi)m_k r^2 + (2H^2 + 4r^2)m_k + a^2m_c + I_2 + I_3) \\ M_b^{2,2} &= \frac{l}{b} (4\cos(\alpha + 2\phi)m_k r^2 - 4\cos(\alpha_c + 2\phi)m_k r^2 + r^2\sin(2\alpha + 4\phi) \\ &- r^2\sin(\alpha + 4\phi + \alpha_c)) \end{split}$$

$$M_b^{3,1} &= 0 \\ M_b^{3,1} &= 0 \\ M_b^{3,2} &= \frac{am_k r^2}{b} \sin(\alpha + 2\phi) \\ M_b^{3,3} &= \frac{1}{b^2} (-m_k r^4 \cos(\alpha + 2\phi)^2 + m_k r^4 - 2I - 2\cos(\alpha_c + 2\phi)r^2 + 2I_2\cos(\alpha_c + 2\phi)r^2 + I_2H^2) \end{split}$$